Journal of Carbon Research

MDPI

Article

$ZnCl_2$-Activated Nanoporous Carbon Materials from *Phyllanthus emblica* Seed for High-Performance Supercapacitors

Lok Kumar Shrestha [1,2,*], Sarita Manandhar [1,2], Sabina Shahi [1,2], Rabindra Nath Acharyya [1,2], Aabha Puri [1,2], Chhabi Lal Gnawali [3,*], Rinita Rajbhandari [3] and Katsuhiko Ariga [1,4]

1 Research Center for Materials Nanoarchitectonics (MANA), National Institute for Materials Science (NIMS), 1-1 Namiki, Tsukuba 305-0044, Ibaraki, Japan; manandhar.sarita@nims.go.jp (S.M.); shahi.sabina@nims.go.jp (S.S.); acharyya.rabindranath@nims.go.jp (R.N.A.); puri.aabha@nims.go.jp (A.P.); ariga.katsuhiko@nims.go.jp (K.A.)
2 Department of Materials Science, Institute of Pure and Applied Sciences, University of Tsukuba, 1-1-1 Tennodai, Tsukuba 305-8573, Ibaraki, Japan
3 Department of Applied Sciences and Chemical Engineering, Pulchowk Campus, Institute of Engineering (IOE), Tribhuvan University, Lalitpur 44700, Nepal; rinita.joshi@pcampus.edu.np
4 Department of Advanced Materials Science, Graduate School of Frontier Sciences, The University of Tokyo, 5-1-5 Kashiwanoha, Kashiwa 277-8561, Chiba, Japan
* Correspondence: shrestha.lokkumar@nims.go.jp (L.K.S.); chhabig123@ioe.edu.np (C.L.G.); Tel.: +81-29-860-4809 (L.K.S.)

Abstract

This study reports the synthesis of an activated nanoporous carbon material from *Phyllanthus emblica* (Amala)—a biomass material which is an eco-friendly, economical, and sustainable precursor used to prepare activated carbon using zinc chloride ($ZnCl_2$) activation at various temperatures (500–700 °C) under a nitrogen gas atmosphere. A sample that was carbonized at 700 °C (AmC_Z700) attained a high specific surface area of 1436 $m^2\ g^{-1}$ and a total pore volume of 0.962 $cm^3\ g^{-1}$, and, when used in an electrode, showed excellent supercapacitance performance, attaining a high specific capacitance of 263 $F\ g^{-1}$ at a current density of 1 $A\ g^{-1}$, followed by 55% capacitance retention at 50 $A\ g^{-1}$. Additionally, the assembled symmetric supercapacitor cell, when operated at 1.2 V, delivered an energy density of 8.9 $Wh\ kg^{-1}$ at a power density of 300 $W\ kg^{-1}$ and exhibited an excellent cycle life of 95% after 10,000 successive charge/discharge cycles, demonstrating the substantial potential of *Phyllanthus emblica* seed-derived carbon materials for the creation of high-performance supercapacitors.

Keywords: biomass carbon; *Phyllanthus emblica*; $ZnCl_2$ activation; hierarchically porous carbons; supercapacitors

Academic Editor: Jorge Bedia

Received: 10 November 2025
Revised: 7 December 2025
Accepted: 11 December 2025
Published: 17 December 2025

Citation: Shrestha, L.K.; Manandhar, S.; Shahi, S.; Acharyya, R.N.; Puri, A.; Gnawali, C.L.; Rajbhandari, R.; Ariga, K. $ZnCl_2$-Activated Nanoporous Carbon Materials from *Phyllanthus emblica* Seed for High-Performance Supercapacitors. *C* **2025**, *11*, 95. https://doi.org/10.3390/c11040095

1. Introduction

The current problems of energy scarcity and environmental pollution, along with rapid advancements in science and technology, have led to a great deal of interest in the urgent development of clean, efficient, and sustainable renewable energy storage systems. Energy storage devices, such as batteries, fuel cells, and supercapacitors, have drawn attention due to their capacity to address the growing energy crisis [1–3]. Among these devices, supercapacitors have drawn the most interest and are highly regarded in fields including electric mobility, portable gadgets, and renewable energy infrastructures because of their exceptional qualities, which include high energy density, quick charge–discharge rates, long lifespans, and environmental friendliness [4–7]. The performance of a supercapacitor's

electrode materials is a major determinant of its effectiveness. These materials should have exceptional electrical conductivity, a high specific surface area, and stable operation. Given their exceptional qualities, such as their high specific surface areas, excellent electrical conductivity, and remarkable structural stability, carbon-based materials are widely recognized as the most appropriate materials for the preparation of electrode materials for supercapacitors [8]. Graphene, carbon nanotubes, fullerenes, crystal-derived carbons, and activated carbons are currently the most widely used carbon electrode materials [9–14]. Supercapacitor development is being hampered by overly complicated and expensive preparation procedures required for these carbon materials. The utilization of agricultural and forestry waste has gained significant interest due to its unique pore structure and elemental composition, which make it a widely accessible, cost-effective resource that meets the requirements for environmental friendliness. Activated carbons with high specific surface areas and hierarchically porous architectures that are derived from natural biomass waste are in great demand for the preparation of electrode materials for supercapacitors [15–20].

Natural biomass precursors are potential candidates for the large-scale production of porous carbon materials that are applicable to wastewater treatment and energy storage supercapacitor applications. Recently, various types of biomass waste materials, like rice husks, cherry stones, Areca catechu nuts, Lapsi (*Choerospondias axillaris*) seeds, tobacco waste, betelnut shells, and many more, have been used as precursor materials for the preparation of porous carbon materials for supercapacitor electrodes [21–29]. For example, Shrestha et al. [30] reported on the creation of nanoporous graphitic carbon materials containing interconnected mesopores from Lapsi seed through zinc chloride activation at 700 °C. The specific surface area and pore volume of the optimal sample were found to be 2272 $m^2\ g^{-1}$ and 2.845 $cm^3\ g^{-1,}$ respectively, suggesting that the sample was superior to commercial activated carbons. Attributed to their high surface areas, well-developed pore structures with interconnected mesopore structures, and large pore volumes, Lapsi seed-derived nanoporous carbon materials have exhibited excellent electrochemical supercapacitance performance, with a maximum specific capacitance of 284 F g^{-1} at a current density of 1 A g^{-1}. Additionally, these electrodes have demonstrated a remarkable cycle life, attaining 99% after 10,000 charge–discharge cycles. Chaiammart et al. [31] synthesized KOH-activated carbon materials from cashew nut shells at different activation temperatures (650, 750, and 850 °C) and achieved a high specific surface of 2034 $m^2\ g^{-1}$. The electrochemical performance of the carbon materials was investigated in 1 M sodium sulphate electrolyte in a three-electrode cell setup. The optimal sample achieved a specific capacitance of 106 F g^{-1} at a current density of 0.5 A $g^{-1,}$ and it retained 75% at 10 A g^{-1} over a 1.0 V potential window. Additionally, a symmetric supercapacitor fabricated from a sample carbonized at 750 °C had an energy density of 2.4 Wh kg^{-1} at a power density of 1002 W kg^{-1}, followed by 87% capacitance retention after 10,000 cycles at 1.0 A g^{-1}. Manandhar and co-workers [32] recently reported the preparation of activated carbon from *Terminalia bellirica* seed stone by chemical activation with $ZnCl_2$. After carbonization at 700–900 °C, the optimal sample exhibited micro/mesoporous structures, a large specific surface area, and suitable nitrogen and oxygen components. The optimal sample as an electrode in supercapacitors achieved an excellent specific capacitance of 365.4 F g^{-1}, with 66% rate capability from 5 mVs^{-1} to 500 mVs^{-1}, and exceptional cycling durability of 98.2% after 10,000 cycles. These examples demonstrated the significant possibilities of natural carbon sources and the activation process that can be used to prepare porous carbon materials for supercapacitor applications. Their availability, affordability, sustainability, and carbon content are the major factors used to select precursor materials.

This study reports on the fabrication of micro/mesoporous carbon materials from *Phyllanthus emblica* seed stones by $ZnCl_2$ activation and their electrochemical energy–storage supercapacitance performance in aqueous electrolyte (1 M H_2SO_4). *Phyllanthus emblica* seed powder was combined with $ZnCl_2$ at a 1:1 ratio (weight ratio) and carbonized at different temperatures (500, 600, and 700 °C) under an inert atmosphere of nitrogen (120 cc min^{-1}) for 4 h. The prepared carbon materials exhibited micro- and mesopore-based hierarchical pore structures. The optimal sample, carbonized at 700 °C, had an excellent specific surface area of 1436 m^2 g^{-1} and a total pore volume of 0.962 cm^3 g^{-1}. Its textural, morphological, and structural analyses reflected good supercapacitance performance. The electrode delivered a high specific capacitance of 262.9 F g^{-1} at 1 A g^{-1} current density and 55% capacitance retention at 50 A g^{-1}. The assembled symmetric cell gave an energy density of 8.9 Wh kg^{-1} at a power density of 300 W kg^{-1} and exhibited an excellent cycle life of 95% after 10,000 successive charge/discharge cycles. These electrochemical results signify the enormous importance of *Phyllanthus emblica* seed for the production of hierarchical porous activated carbons at a low cost, which is highly demanded for energy storage supercapacitor applications.

2. Materials and Methods

2.1. Materials

Phyllanthus emblica (locally known as Amala) fruit was purchased from a local market. The activator zinc chloride ($ZnCl_2$: 99.5%) was purchased from Nacali Tesque Inc., Kyoto, Japan. Hydrochloric acid solution (1 M) and sulfuric acid solution (1 M) were also obtained from Nacali Tesque Inc., Kyoto, Japan. For washing samples and preparing solutions, Millipore filtered water was used.

2.2. Preparation of Nanoporous Carbon Materials

Phyllanthus emblica (Amala) seed was washed with Milli-Q filtered water, dried at 100 °C for 24 h in a hot air oven, ground into powder form on a mechanical crusher, and sieved through a 300 μm mesh. The sieved precursor powder was mixed with $ZnCl_2$ in an agate mortar in a ratio of 1:1 by weight and kept at 25 °C for 24 h. The mixture was carbonized in a tube furnace at different carbonization temperatures (500, 600, and 700 °C) under a continuous flow of nitrogen gas (120 cc min^{-1}) for a hold time of 4 h. The zinc chloride-activated carbons were cooled to room temperature, treated with 0.1 M hydrochloric acid solution, and repeatedly washed with distilled water until the supernatant liquid attained a pH of ~7 and were then dried at 120 °C for 12 h. Then, the activated carbons prepared from *Phyllanthus emblica* (Amala) at 500, 600, and 700 °C were designated as AmC_Z500, AmC_Z600, and AmC_Z700. The yields of the prepared samples were ca. 45.0% (AmC_Z500), 44% (AmC_Z600), and 43.3% (AmC_Z700). The directly carbonized reference sample was prepared in a tube furnace in an inert atmosphere of nitrogen gas for 4 h at 500 °C without zinc chloride activation and labeled as AmP_500.

2.3. Characterizations

Surface functionality and the pyrolytic decomposition of the precursor powder were investigated by using infrared (FTIR) spectrophotometry and thermogravimetry (TGA). The ATR-FTIR spectrum was recorded using a NICOLET iS20 (Thermo-Fisher Scientific, Waltham, MA, USA), and the TGA curve was recorded under a nitrogen environment using a STA 2500, Regulus, NETZSCH, Selb, Germany, from 25 to 1000 °C at a temperature ramp of 10 °C min^{-1}. Surface textural properties, including total specific surface area, pore size distribution, and total pore volumes of the prepared carbon materials, including the directly carbonized reference samples, were studied by nitrogen gas adsorption, recording

the adsorption isotherm on a Quantachrome Autosorb-iQ2, Boynton Beach, FL, USA. Micropore and mesopore size distribution profiles were obtained by the non-linear density functional theory NDFT (for micropores) and the Barrett–Joyner–Halenda (BJH) model (for mesopores). For the structural characterizations, powder X-ray diffraction (XRD) (Rigaku X-ray diffractometer, RINT, Tokyo, Japan), Raman scattering (NRS-3100, JASCO, Tokyo, Japan), scanning electron microscopy (SEM: S-4800, Hitachi Co., Ltd., Tokyo, Japan) and transmission electron microscopy (TEM: Talso F200X G2 Thermo Fisher Scientific operated at 200 kV) were used.

2.4. Electrochemical Properties

The electrochemical supercapacitance performance of the Amala seed-derived porous carbon materials was studied by cyclic voltammetry (CV), galvanostatic charge/discharge (GCD), and electrochemical impedance spectroscopy (EIS) measurements in an aqueous 1 M H_2SO_4 electrolyte solution in three-electrode and two-electrode cell setups. First of all, the working electrode was fabricated on a clean and dry graphite sheet (1 × 3 cm^2). The Amala carbon was ground into a fine powder and mixed with a binder poly(vinylidene fluoride) (PVDF), and a conductive matrix, carbon black, at a mixing ratio of 80:10:10 by weight. A slurry of the above mixture was prepared with N-methyl-2-pyrrolidone (NMP), and the slurry was coated on the graphite sheet (1 × 1 cm^2), followed by drying at 80 °C overnight. The mass of active electrode material was ~1.6 mg. CV, GCD, and EIS measurements were performed using a Biologic potentiostat (Bio-Logic SAS, model VSP-3e, Seyssinet-Pariset, France). Ag/AgCl and platinum (Pt) wire were the reference and counter electrodes, respectively. The specific capacitance (C_S) of the electrodes was calculated using Equation (1):

$$C_s = \frac{I \times t_d}{m \times \Delta V} \quad (1)$$

I (A), t_d (s), m (g), and ΔV (V) in Equation (1) are discharge current, discharge time, mass of active electrode material, and operating voltage, respectively.

The surface-controlled and diffusion-controlled contributions were studied from the cyclic voltammograms to understand the charge–discharge dynamics. The scan rate (ν) and current density (i) are related according to Equation (2):

$$i = a\nu^b \quad (2)$$

where i (A g^{-1}) is the sum of the current contributions of the surface-controlled (capacitive) and diffusion-controlled currents. a and b are constants, and ν is the scan rate (mV s^{-1}). If the value of $b \approx 1$, the surface-controlled process leads the charge storage mechanism, as is typical for EDLC or pseudo-capacitance. If the value of $b \approx 0.5$, the diffusion-controlled mechanism dominates. The current collection is governed by the diffusion of electrolyte ions within the bulk of the electrode material. The surface- and diffusion-controlled current contributions can be calculated quantitatively using Equation (3):

$$i(V) = k_1\nu + k_2\nu^{1/2} \quad (3)$$

where i, ν, k_1, and k_2 are total current, scan rate, and constants, respectively.

For symmetric supercapacitor cells (two-electrode system), the energy density (E: Wh kg^{-1}) and power density (P: W kg^{-1}) can be calculated using the following equations:

$$E = \frac{0.5 \times C_s \times (\Delta V)^2}{3.6} \quad (4)$$

$$P = \frac{3600 \times E}{t_d} \quad (5)$$

3. Results and Discussion

The FTIR spectrum (Figure 1a) of the precursor *Phyllanthus emblica* (Amala) seed powder indicates the oxygenated surface functional groups that correspond to the cellulose, hemicellulose, and lignin present in the precursor. A pronounced peak at 3339 cm^{-1} is associated with the O-H (str.) of moisture water and/or the alcoholic group of the cellulose, while the bands at 2924 cm^{-1} and 2853 cm^{-1} correspond to the aliphatic C-H (str.) of the cellulose. The band at 1729 cm^{-1} was assigned to the C-O (str.) of unsaturated ester, whereas the weak bands around 1635 cm^{-1} and 1620 cm^{-1} indicate that the moisture water in the precursor corresponds to O-H (def.) and C=C (str.), respectively [33–35]. Several peaks were observed in the range of 1600–1000 cm^{-1}, corresponding to C-H (def.) and C-O (str.). These peaks indicated cellulose and lignin, which are the main components of lignocellulosic materials [36].

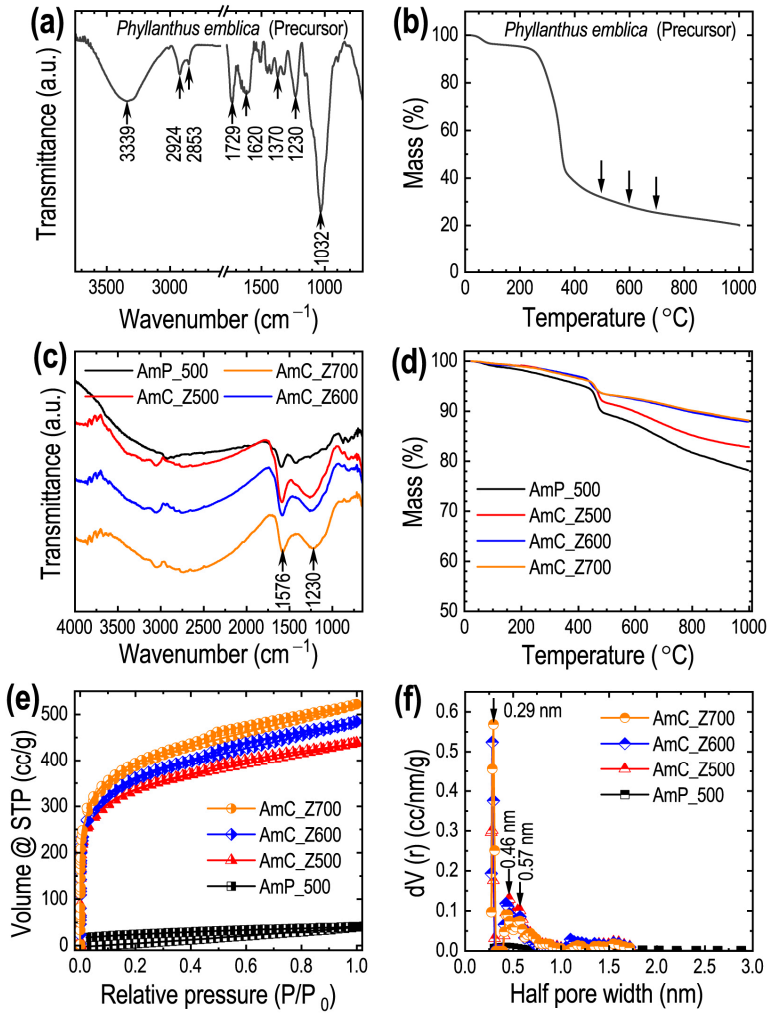

Figure 1. (**a**) The FTIR spectrum and (**b**) TGA curve of *Phyllanthus emblica* seed powder; (**c**) FTIR spectra and (**d**) TGA curves of the carbonized samples; (**e**) nitrogen adsorption isotherms and (**f**) pore size distribution profiles of the directly carbonized reference sample (AmP_500) and the $ZnCl_2$-activated carbon materials, (AmC_Z500, AmC_Z600, and AmC_Z700).

From the TGA curve, it can be seen that the decomposition of *Phyllanthus emblica* seed powder takes place in three different stages (Figure 1b). The first stage is below 200 °C,

where a slight weight loss can be attributed to the drying up of moisture or crystallized water. In the second stage, in the temperature range of 200–400 °C, the gases/volatile compounds are released, and a significant weight loss (~65%) is observed (Figure 1b), which may be due to the polymerization of cellulose and hemicellulose and the degradation of carbohydrates. In the third stage, above 400 °C, there is no significant mass loss, indicating the slow decomposition of higher-molecular-weight lignin into carbon. This suggests that a suitable temperature for carbonization is above 400 °C [37]. Hence, the $ZnCl_2$ activation of Amala seed powder was performed at 500, 600, and 700 °C. The oxygenated surface functionality was sustained in the carbonized samples (Figure 1c). The presence of the FTIR band at 1230 cm^{-1} resembles the C-O stretching vibration, while the peak at 1576 cm^{-1} is due to the C=C stretching vibrations in the aromatic rings. TGA curves of the carbonized samples show better thermal stability at higher carbonization temperature (Figure 1d).

The surface textural properties were investigated by nitrogen adsorption isotherms. The isotherm of the reference sample (directly carbonized) and the activated samples carbonized at various carbonization temperatures are displayed in Figure 1c. The reference sample AmP_500 exhibits a type-III adsorption isotherm, suggesting the absence of well-defined porosity. This sample is mostly nonporous or has only macropores. Because of their hierarchical micro- and mesoporous structure, all the $ZnCl_2$-activated carbon materials adsorbed nitrogen strongly at lower relative pressure and exhibited a hysteresis loop at higher relative pressure, indicating mixed type-I and type-IV isotherms [38–40]. At low relative pressure, high nitrogen adsorption is caused by micropore filling. The hysteresis loop observed at higher relative pressure can be attributed to the capillary condensation occurring in the mesopores. It has been observed that the rise in carbonization temperature causes a fall in the integrated area of the hysteresis loop. However, nitrogen adsorption seems to increase at lower relative pressure, suggesting that more micropores and fewer mesopores were formed on the samples prepared at higher temperatures. The specific surface area of the sample AmC_Z700, carbonized at 700 °C, is the highest (1436 m^2 g^{-1}), as compared to the directly carbonized sample AmP_500, signifying that activation plays a crucial role in increasing the surface area/porosity of the carbon samples. Figure 1d shows the micropore size distribution, and Figure S1 (Supporting Information) shows the mesopore size distribution. These results demonstrate the hierarchical micro-and mesopore structures present in the prepared carbon materials.

Table 1 summarizes the surface areas, pore volumes, and pore sizes of all the prepared samples from *Phyllanthus emblica* and shows how temperature has a vital influence on the creation of pore structure in ZnCl2-activated carbon. Carbon materials with this pore structure play a crucial role in adsorption and electrolyte-ion transfer. From Table 1, it is seen that the sample with the highest surface area (AmC_Z700) has an average mesopore diameter of 3.68 nm, with an average half pore width of 0.295 nm and a total pore volume of 0.962 cm^3 g^{-1}. It is further noted that with the increase in carbonization temperature from 500 to 700 °C, the micropore surface area increases continuously due to the creation of a large number of microporous structures. On the other hand, the mesopore surface area remains unchanged at and above 600 °C, suggesting that low-temperature carbonization is insufficient for the coalescence of micropores.

Table 1. Textural properties of Amala seed-derived porous carbon materials *.

System	*SSA* ($m^2\ g^{-1}$)	S_{micro} ($m^2\ g^{-1}$)	S_{meso} ($m^2\ g^{-1}$)	V_p ($cm^3\ g^{-1}$)	V_{micro} ($cm^3\ g^{-1}$)	V_{meso} ($cm^3\ g^{-1}$)	V_{mic}/V_p (%)	V_{mes}/V_p (%)	W_p (nm)	D_P (nm)
AmP_500	100.7	80.0	20.7	0.096	0.066	0.030	68.75	31.25	----	3.82
AmC_Z500	1285.6	1150.9	134.7	0.800	0.623	0.177	77.87	22.13	0.295	3.68
AmC_Z600	1349.2	1188.2	161.0	0.902	0.689	0.213	76.38	23.62	0.283	3.68
AmC_Z700	1436.3	1270.9	165.4	0.962	0.744	0.218	77.34	22.66	0.283	3.69

* *SSA* = total specific surface area, S_{micro} = micropore surface area, S_{meso} = mesopore surface area, V_p = total pore volume, V_{micro} = volume of micropores, V_{micro} = volume of mesopore, V_{mic}/V_p = micropore volume fraction, V_{meso}/V_p = mesopore volume fraction, W_p= average half-pore width, and D_p = average pore diameter.

The surface morphology of the prepared carbon materials was studied by SEM observations. Figure 2 shows the SEM images of the directly carbonized reference sample and the ZnCl2-activated carbon materials. Formation of irregular-shaped micron-sized carbon particles with random dimensions can be seen in the low-resolution SEM images (Figure 2a,d,g,j). Semi-high resolution SEM images (Figure 2b,e,h,k) show a channel-like morphology with non-uniform macroporous structures, which is often observed in biomass-derived activated carbon. High-resolution SEM images (Figure 2f,i,l) of the activated carbon samples reveal a well-developed mesoporous structure randomly distributed over the surface of the carbon particles. These SEM images show that the porosity of the materials improves with increasing carbonization temperature. High-resolution SEM images reveal that high-porosity carbon materials were formed during activation at higher temperatures. However, a pore structure was not developed in the directly carbonized reference sample (Figure 2b,c). This suggests that the activating agent plays a crucial role in the development of micro- and mesoporous structures. The additional SEM images are supplied in the Supporting Information: AmP_500 (Figure S2), AmC_Z500 (Figure S3), AmC_Z600 (Figure S4), and AmC_Z700 (Figure S5).

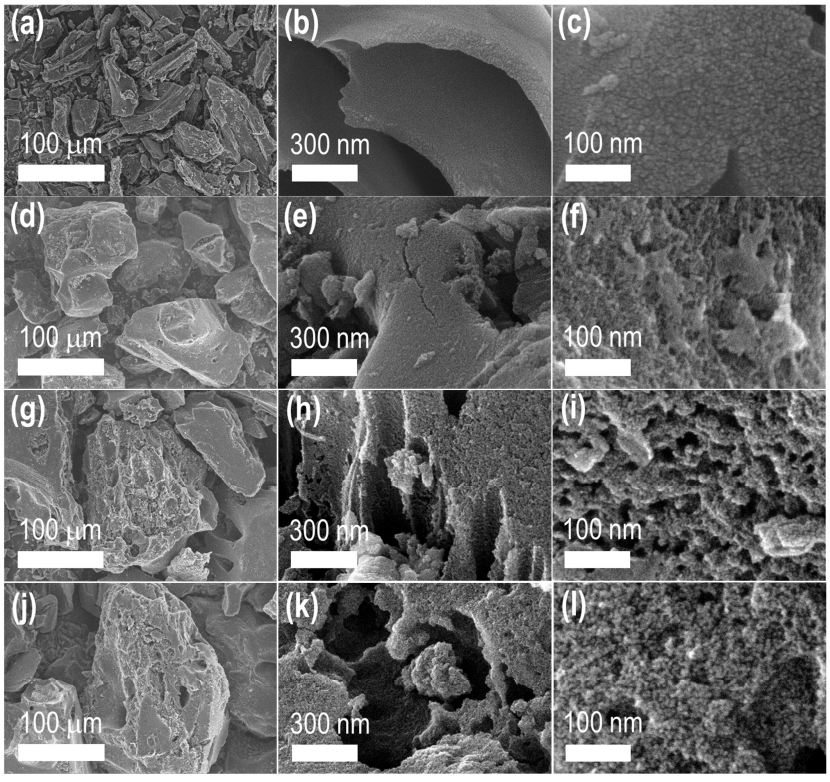

Figure 2. SEM images of (**a**–**c**) AmP_500, (**d**–**f**) AmC_Z500, (**g**–**i**) AmC_Z600, and (**j**–**l**) AmC_Z700.

Figure 3 shows TEM images of the optimal sample, AmC_Z700. The hierarchical porous structure can be seen to have both meso-and microporous architectures, referring to the internal porous structure of the carbon materials. A nanoporous structure can be seen in the TEM images (Figure 3a,b), while the HR-TEM images (Figure 3c,d) reveal a microporous carbon structure with randomly developed graphitic carbon layers [41]. Plenty of micropores, as highlighted by dotted circles, can be seen. These nanoporous structures in the carbon skeleton are formed due to the gasification/or release of volatile organic compounds during carbonization of *Phyllanthus emblica* seed powder at high temperatures.

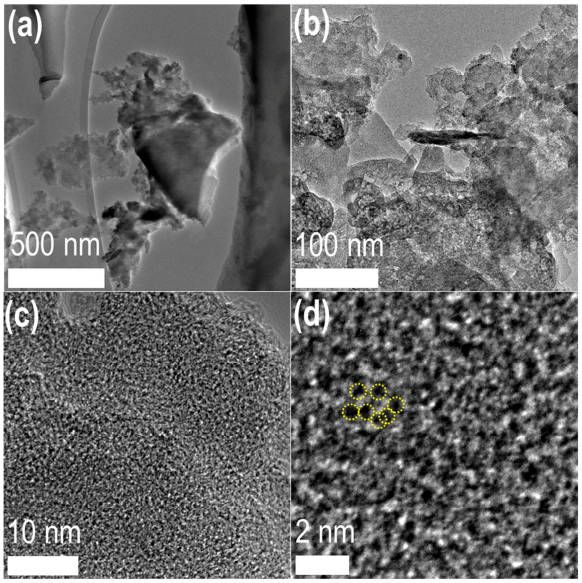

Figure 3. (**a**,**b**) TEM and (**c**,**d**) HR-TEM images of AmC_Z700. Dotted circles in panel (**d**) highlight the micropores as a typical example.

The structure of all porous carbon materials derived from *Phyllanthus emblica* seed was further studied using powder XRD and Raman scattering spectroscopy. Figure 4a shows the XRD patterns of all the activated carbons as well as the directly carbonized reference sample. As seen in Figure 4a, the XRD patterns of all the samples reveal two diffraction bands that occur at diffraction angles of 24.7 and 43.4°. These two peaks correspond to the (002) and (100) planes of amorphous carbons caused by the disordered graphitic structures. This type of amorphous structure is commonly observed in activated carbons derived from biomass [42].

The Raman scattering spectra of all the prepared samples are shown in Figure 4b. The spectra of all the samples exhibit two characteristic peaks at ~1340 cm^{-1} and ~1595 cm^{-1}. These peaks correspond to the defect or disorder (*D* band) and graphitic (*G* band) structures in the carbon, which are characteristics of amorphous carbon [43]. The degree of graphitization of carbon materials can be estimated by calculating the ratio of intensities of the *G* and *D* bands (I_G/I_D). The value of I_G/I_D is ca. 1.25 for the reference sample, showing a good degree of graphitization, which can be attributed to the complex composition of the precursor, containing several minerals that can catalyze graphitization during direct carbonization. The value of I_G/I_D remains apparently unchanged and ca. ~1.10 in the activated samples, implying a similar degree of graphitization in the samples carbonized from 500 to 700 °C. The graphitic structure influences electrical conductivity, specific surface area, and pore size, which influence the performance of carbon materials in separation and energy storage systems.

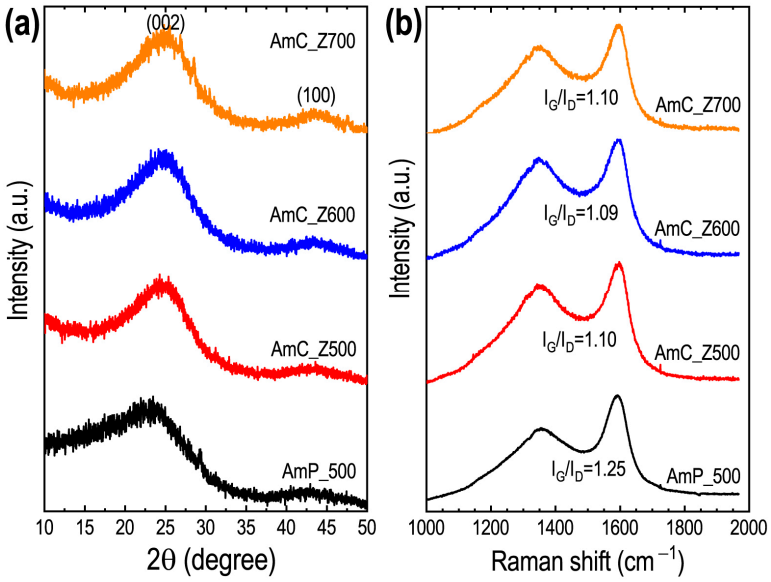

Figure 4. (**a**) Powder XRD patterns and (**b**) Raman scattering spectra of AmP_500, AmC_Z500, AmC_Z600, and AmC_Z700.

The excellent surface textural properties of the hierarchical micro- and mesoporous structures of the *Phyllanthus emblica* seed-derived carbon materials motivated us to study the electrochemical supercapacitance performance of the prepared carbon materials. Figure 5a compares the CV curves of the ZnCl2-activated carbon samples with a directly carbonized reference sample at a fixed potential sweep of 50 mVs^{-1}.

The quasi-rectangular CV profiles of all the samples suggest an EDLC-type energy storage mechanism, as observed in other carbon-based electrodes [44,45]. The weak redox peaks observed at approximately 0.2–0.4 V in the CV curves of AmC_Z600 and AmC_Z700 (Figure 5a) can be attributed to the partial contribution of pseudo-capacitance; this may be due to the presence of oxygen functionalities in these samples. It is observed that the total internal current of the reference sample AmP_500 is low, which is due to its lack of porosity, and it increases with an increase in carbonization temperature. The sample AmC_Z700 exhibits the highest current collection, indicating that it has the maximum energy storage capacity among these materials. This is consistent with its surface area, i.e., carbons with higher specific surface areas have superior energy storage properties. The CV curves recorded for the reference sample (Figure 5b) and the activated carbon samples AmC_Z600 (Figure 5c) and AmC_Z700 (Figure 5d), across a wide range of potential sweeps (5–500 mVs^{-1}), show that the current output increases with the increasing potential sweep. The sustained quasi-rectangular CV curve, even at a higher potential sweep, suggests an enhanced electrolyte ion diffusion through the mesoporous channels in the electrode materials [46]. The plot between log (ν) and log (i) of the AmC_Z700 electrode gives a *b* value of 0.93 as calculated using Equation (2) (Figure 5e). This indicates that the charge storage mechanism is dominantly surface-controlled, as is commonly observed in hierarchically porous carbon materials. A capacitance contribution analysis shows that the surface-controlled process is superior to the diffusion-controlled process over the entire potential sweep (Figure 5f).

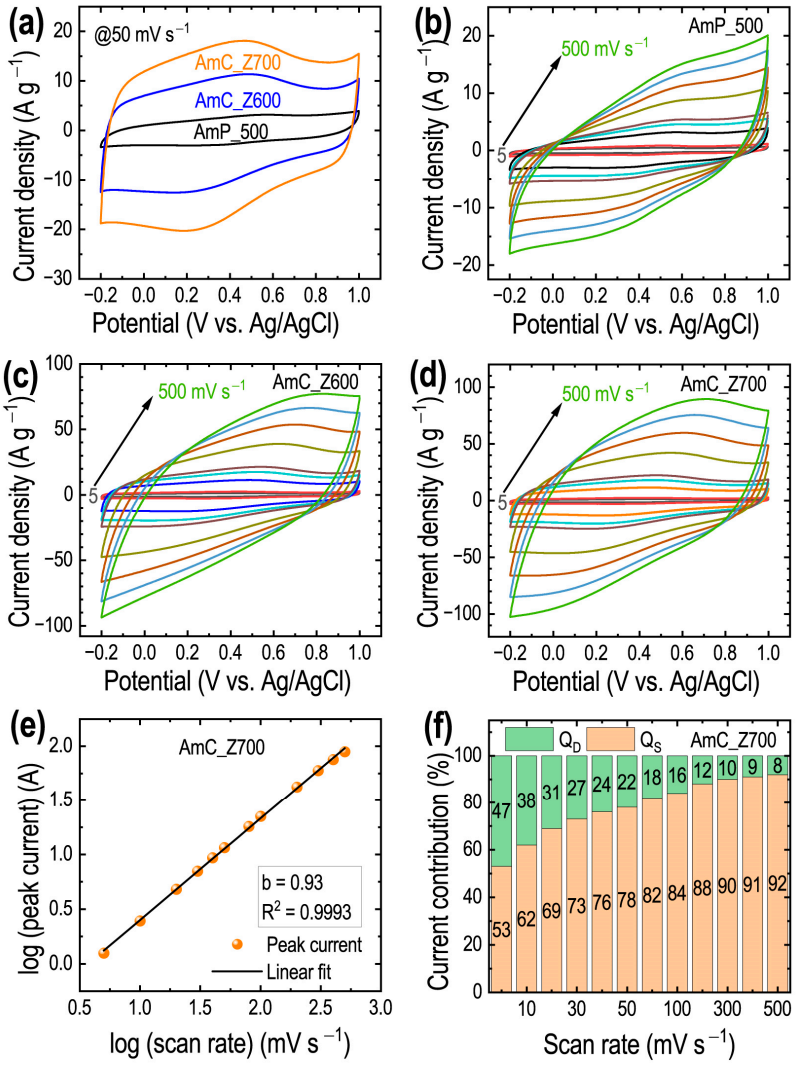

Figure 5. CV profiles of carbon materials derived from Amala seed stone. (**a**) CV response at a fixed scan rate of 50 mVs^{-1}, CV profiles at different scan rates (5, 10, 50, 80, 100, 200, 300, 400, and 500 mVs^{-1}) for (**b**) AmP_500, (**c**) AmC-Z600, and (**d**) AmC-Z700, (**e**) logarithm of the oxidative peak current vs. scan rate of the AmC_Z700 sample, and (**f**) the corresponding surface-controlled (Q_S) and diffusion-controlled (Q_D) contributions.

Supercapacitance performance was also studied by measuring the GCD curves in three-electrode systems at different current densities (1 to 50 A g^{-1}). Figure 6a compares the GCD profiles of all the carbon materials at a fixed current density of 1 A g^{-1}, which are of triangular shape, confirming the EDLC-type charge storage mechanism [47–49]. In GCD curves, the discharge time determines the ability of the electrode to store energy (Equation (1)), which is influenced by its surface area and pore size. As observed from the GCD curve, the discharge time of the directly carbonized reference sample is the shortest, and hence it has a poor specific capacitance because of its lack of porosity. Conversely, due to its well-developed nanoporous structure, the sample with the best surface area and porosity (AmC_Z700) has the longest discharge time, indicating that it has the highest charge storage capacity. The specific capacitance of the sample with optimal specific surface area (AmC_Z700) was calculated as 263 F g^{-1} at 1 A g^{-1}, which is higher or comparable to several other biomass carbon materials (see Tables S1 and S2 in the Supporting Information) [30,50–69].

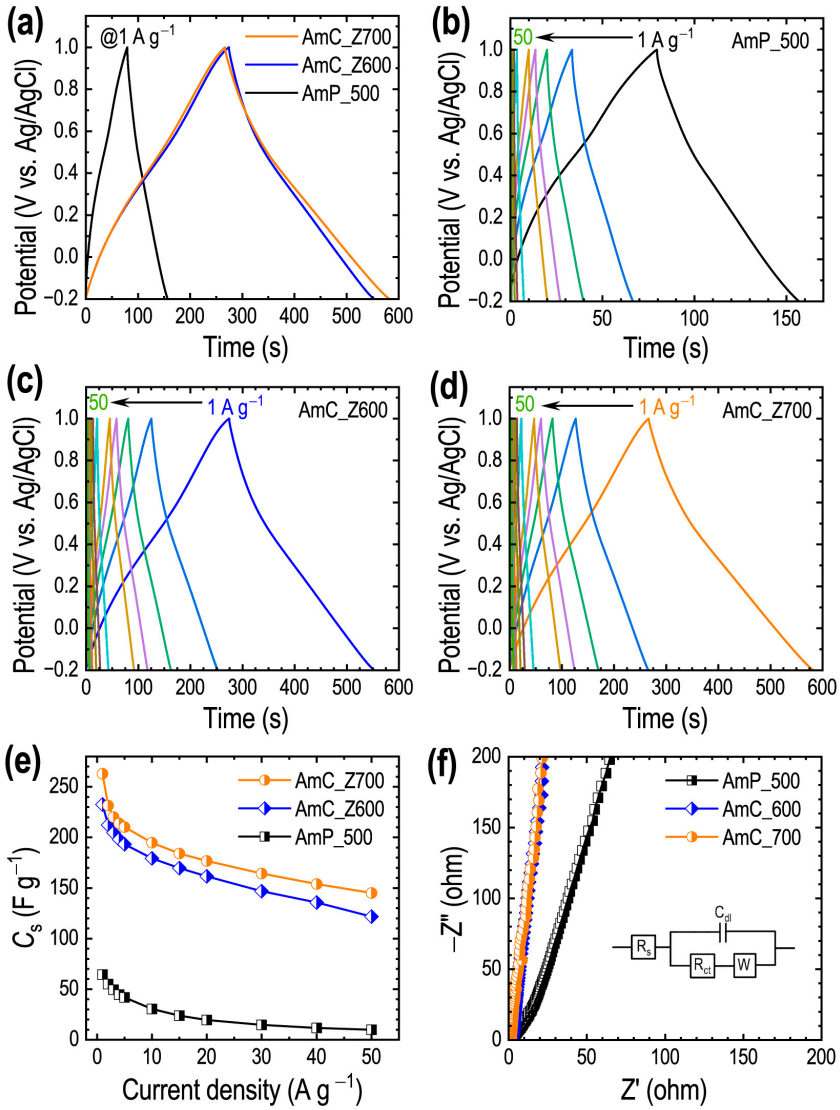

Figure 6. (**a**) Comparison of the GCD profiles of the reference AmP_500 sample and the $ZnCl_2$-activated carbon materials AmC_Z600 and AmC_Z700 at 1 A g^{-1}, (**b**) GCD vs. the current density profile of AmP_500 at different current densities (1, 2, 3, 4, 5, 10, 15, 20, 30, 40, and 50 A g^{-1}), (**c**) GCD vs. the current density profile of AmC_Z600, (**d**) GCD vs. the current density profile of AmC_Z700, (**e**) calculated specific capacitance vs. current density profiles, (**f**) Nyquist plots with equivalent circuits of the AmP_500, AmC_Z600, and AmC_Z700 samples.

The sample that was carbonized at a lower carbonization temperature exhibited a specific capacitance of 232 F g^{-1} (AmC_Z600). The specific capacitance of the directly carbonized sample (AmP_500) was only 64 F g^{-1} at 1 A g^{-1} due to its lack of porosity. The GCD curves of the directly carbonized (Figure 6b) and activated samples AmC_Z600 (Figure 6c), AmC_Z700 (Figure 6d) all maintained a triangular shape at high current density, confirming the effective diffusion mechanism within the interior of the electrodes through the mesopores. Both of the activated samples showed good performance rates, sustaining 55% (AmC_Z700) and 52% (AmC_Z600) capacitance retention at a high current density of 50 A g^{-1} (Figure S6), implying the potential of these materials to be used in high-rate performance supercapacitor devices. Figure 6f shows Nyquist plots that correlate the electron-transfer kinetics, electrolyte-ion diffusion kinetics, and double-layer charging of these materials at the electrode surface. The Nyquist plots are typical of carbon materials with a dominance of EDLC behavior [4,8,16,20,32]. All the samples exhibited apparently similar behavior at both high (Figure S7) and low frequencies (Figure 6f),

implying similar equivalent series resistance and rapid electron transfer to the electrode surface. Therefore, the difference in their specific capacitances can be attributed to the surface textural properties of the electrode materials.

The sample with the optimal surface textural properties, AmC_Z700, showed the best energy storage performance. Therefore, a symmetrical cell was assembled with AmC_Z700 to study its energy density performance. The CV profile of the cell at different scan rates in the potential window of 1.2 V is a rectangular curve, demonstrating the EDLC character of the cell (Figure 7a). The CV curve departs slightly from the ideal rectangular shape as the scan rate increases due to charge transport resistance. The GCD profile (Figure 7b) of the cell at different current densities shows an almost triangular shape, indicating an EDLC charge storage mechanism. The cell has low resistance, as indicated by the absence of a voltage (IR) drop. The C_s of the cell vs. the current density curve (Figure 7c) indicates that the cell has high capacitance retention (48%) at 50 A g^{-1} (a high current density), showing its high-rate capability. Figure 7d shows the Nyquist plot. The semicircle observed at high frequency reflects the charge-transfer processes occurring at the electrode–electrolyte interface [70]. A small semicircle indicates lower charge transfer resistance, which may be due to the good conductivity of the prepared carbon. The linear region at lower frequencies is associated with the diffusion of ions/ion transport limitation. The near-vertical line in the low-frequency region represents the capacitive behavior of the electrical double layer formed at the electrode/electrolyte interface. The value of the equivalent series resistance (ESR) is ca. 0.279 Ω, and the charge-transfer resistance is ca. 0.721 Ω, indicating favorable electrical conductivity.

The cyclic life of the cell (Figure 7e), measured at 10 A g^{-1}, shows outstanding cycling performance, sustaining 95% capacitance and 100% coulombic efficiency even after 10,000 charge/discharge cycles. The charge storage process is highly reversible and non-faradaic with fast ion transport that leads to negligible material degradation and consistent performance over a long cycle life. This shows that the material is highly stable with no/minimal degradation in the electrode–electrolyte interface. Energy density is a significantly useful measure to analyze a supercapacitor's energy storage performance and is represented in the Ragone plot (Figure 7f). The cell delivered a maximum energy density of 8.9 Wh kg^{-1} at a power density of 300 W kg^{-1}, which is better than/comparable to previously mentioned biomass-derived carbon compounds [71–74]. A comparative table of the energy performance of *Phyllanthus emblica* carbon with similar other biomass-derived carbon materials is supplied in Table S2 [28,75–81].

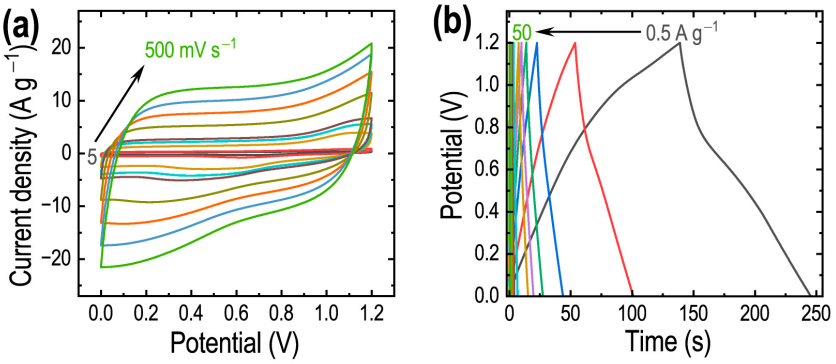

Figure 7. *Cont.*

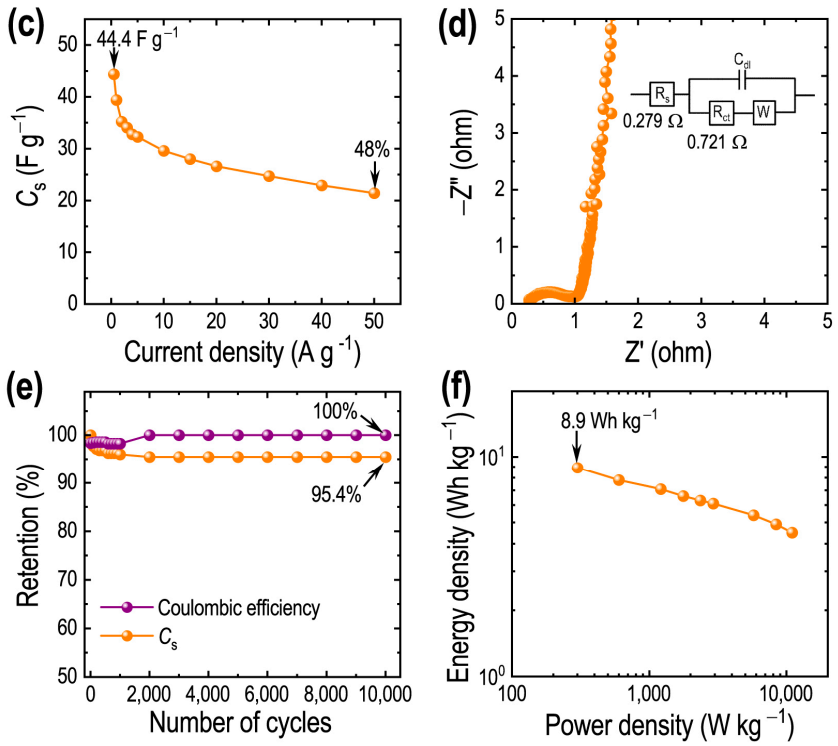

Figure 7. Electrochemical supercapacitance performance of the assembled symmetric supercapacitor cell using the AmC_Z700 sample in an aqueous 1 M H_2SO_4 solution. (**a**) CV curves vs. scan rates (5, 10, 50, 80, 100, 200, 300, 400, and 500 mV s^{-1}); (**b**) GCD profiles vs. current densities (0.5, 1, 2, 3, 4, 5, 10, 15, 20, 30, 40, and 50 A g^{-1}); (**c**) calculated specific capacitance; (**d**) Nyquist plot obtained from the EIS measurement with equivalent circuit diagram; (**e**) cycle performance with coulombic efficiency at a current density of 10 A g^{-1}; and (**f**) Ragone plot of the symmetric cell.

4. Conclusions

In summary, we have synthesized hierarchically nanoporous activated carbons with high surface areas from the precursor *Phyllanthus emblica* under a nitrogen gas atmosphere at different carbonization temperatures, ranging from 500 to 700 °C, by chemical activation with $ZnCl_2$. The electrical double-layer supercapacitance performance of these carbons was measured in a three-electrode cell setup in an aqueous solution (1 M H_2SO_4). $ZnCl_2$-activated *Phyllanthus emblica* seed-derived carbon materials exhibited excellent surface textural properties. Their surface areas ranged from 1285 to 1436 m^2 g^{-1}, and their total pore volumes ranged from 0.800 to 0.962 cm^3 g^{-1}. The sample with optimal surface textural properties (AmC_Z700) achieved an excellent specific capacitance of 263 F g^{-1} at a current density of 1 A g^{-1} and sustained 55% capacitance even at a high current density of 50 A g^{-1}. The assembled symmetric supercapacitor cell, when operated at 1.2 V, offered a good energy density of 8.9 Wh kg^{-1} and a power density of 300 W kg^{-1}. It sustained 4.5 Wh kg^{-1} energy density at a high-power density of 11,000 W kg^{-1}. Additionally, the cell showed excellent cycle life, with 95% and 100% coulombic efficiency after 10,000 successive charge/discharge cycles, signifying the potential impact of *Phyllanthus emblica* seed on the scalable production of nanoporous carbon materials, which is applicable for high-performance supercapacitor applications. The electrochemical supercapacitance performance of recent nanoporous carbon materials has demonstrated the key roles of various parameters, including surface textural properties, hierarchical pore structures, pore interconnectivity, heteroatom doping, chemical stability, and electrode material conductivity. The overall physicochemical properties of electrode materials depend on the starting materials. Biomass represents a low-cost and sustainable material. Nevertheless, due to the complexity of its composition, its energy

performance remains poor compared to other pseudocapacitive materials, including MOF, MXenes, and redox metal oxide and their composites [82–86]. One strategy would be to integrate MOF, MXene, and redox species into ultrahigh-surface-area functional porous carbon to realize a synergy between EDLC and pseudocapacitance, thereby enhancing the energy performance of supercapacitors.

Supplementary Materials: The following supporting information can be downloaded at: https://www.mdpi.com/article/10.3390/c11040095/s1, Figure S1: Pore size distribution profiles obtained through the BJH method; Figure S2: Additional SEM images of AmP_500; Figure S3: Additional SEM images of AmC_Z500; Figure S4: Additional SEM images of AmC_Z600; Figure S5: Additional SEM images of AmC_Z700; Figure S6: Capacitance retention curves for AmP_500, AmC_Z600, and AmC_Z700; Figure S7: Nyquist plots at high-frequency region; Table S1: Comparison of specific capacitance of Amala carbon with other biomass carbons. Table S2: Energy performance of Phyllanthus emblica carbon with similar other biomass carbon materials.

Author Contributions: Conceptualization, L.K.S.; methodology, L.K.S., S.M., S.S., R.N.A., A.P., C.L.G. and R.R.; validation, L.K.S., formal analysis, L.K.S., S.M. and S.S.; investigation, L.K.S., S.M., S.S., C.L.G., R.N.A., A.P. and R.R.; resources, L.K.S. and K.A.; data curation, L.K.S. and S.S.; writing—original draft preparation, C.L.G. and S.S.; writing—review and editing, L.K.S. and K.A.; visualization, L.K.S. and K.A.; supervision, L.K.S.; project administration, L.K.S. and K.A.; funding acquisition L.K.S. and K.A. All authors have read and agreed to the published version of the manuscript.

Funding: This work was partially supported by JSPS KAKENHI Grant Numbers JP23H05459 and JP25H00898.

Data Availability Statement: The original contributions presented in this study are included in the article/Supplementary Material. Further inquiries can be directed to the corresponding authors.

Acknowledgments: S.S. and R.N.A. are thankful to the Ministry of Education, Culture, Sports, Science and Technology (MEXT) for the doctoral program scholarship. S.M. and A.P. are thankful to the National Institute for Materials Science (NIMS), Japan for the NIMS Junior Research Fellowship.

Conflicts of Interest: The authors declare no conflicts of interest.

References

1. Shu, X.; Yang, Y.; Yang, Z.; Wang, H.; Yu, N. A Nitrogen/Oxygen Dual-Doped Porous Carbon with High Catalytic Conversion Ability toward Polysulfides for Advanced Lithium–Sulfur Batteries. *C* **2024**, *10*, 67. [CrossRef]
2. Marinoiu, A.; Iordache, M.; Borta, E.S.; Oubraham, A. Graphene-Based Nanostructured Cathodes for Polymer Electrolyte Membrane Fuel Cells with Increased Resource. *C* **2024**, *10*, 105. [CrossRef]
3. Simon, P.; Gogotsi, Y. Perspective for Electrochemical Capacitors and Related Devices. *Nature Mater.* **2020**, *19*, 1151–1163. [CrossRef] [PubMed]
4. Zhao, J.; Wang, R.; Yue, L.; Wang, J.; Mi, J.; Boymirzayev, A.; Shodmanov, J.; Feng, Y. Tuning Charge Storage Mechanisms in Carbon Nanofibers via Activator Chemistry: A Path to High-Performance Supercapacitors. *Carbon* **2026**, *247*, 120915. [CrossRef]
5. Bo, W.; Zhang, H.; Yin, G.; Zhang, L.; Qin, J. Recent Advances in Graphene-Based Mesoporous Nanosheets for Supercapacitors. *C* **2023**, *9*, 91. [CrossRef]
6. Qiao, Z.; Bian, K.; Ding, C.; Zhao, Y. Recent Progress of Carbon-Fiber-Based Electrode Materials for Energy Storage. *Diamond Relat. Mater.* **2023**, *138*, 110208. [CrossRef]
7. Shrestha, R.G.; Shrestha, L.K.; Ariga, K. Carbon Nanoarchitectonics for Energy and Related Applications. *C* **2021**, *7*, 73. [CrossRef]
8. Kang, Z.; Xu, D.; Zhao, L.; Liu, D. Boosting Supercapacitor Performance with High-Specific Surface Area Porous Carbon Derived from Sugarcane Bagasse. *J. Energy Storage* **2024**, *104*, 114718. [CrossRef]
9. Ding, T.; Jiang, X.; Quan, J.; Wang, R.; Li, W.; Li, M.; Lan, C.; Ma, W.; Zhu, M. Scalable Fabrication of Hierarchically Porous Graphene Fibers via Hydrothermal Self-Assembly and GO-Assisted Wet-Spinning for High-Performance Flexible Supercapacitors. *Carbon* **2025**, *239*, 120326. [CrossRef]
10. George, N.S.; Bahadur, R.; Fawaz, M.; Tahery, S.; Munroe, P.; Aravind, A.; Sajan, D.; Singh, G.; Vinu, A. Carbon Nitride Incorporated Nanoporous Carbon Nanoarchitectonics Derived from Victorian Brown Coal for Supercapacitor and Oxygen Reduction Reaction. *Carbon* **2025**, *256*, 120857. [CrossRef]

11. Muangrat, W.; Obata, M.; Htay, M.T.; Fujishige, M.; Dulyaseree, P.; Wongwiriyapan, W.; Hashimoto, Y. Nitrogen-Doped Graphene Nanosheet-Double-Walled Carbon Nanotube Hybrid Nanostructures for High-Performance Supercapacitors. *FlatChem* **2021**, *29*, 100292. [CrossRef]
12. Stanley, J.T.; Shinde, P.A.; Ma, R.; Hill, J.P.; Ariga, K.; Subramanian, S.; Shrestha, L.K. Nanoarchitectonic Grafting of NiCo-Layered Double Hydroxide on Fullerene-Derived Carbon Nanorods for Hybrid Supercapacitors. *Carbon* **2025**, *244*, 120642. [CrossRef]
13. Shrestha, R.G.; Maji, S.; Shrestha, L.K.; Ariga, K. Nanoarchitectonics of Nanoporous Carbon Materials in Supercapacitors Applications. *Nanomaterials* **2020**, *10*, 639. [CrossRef]
14. Jia, H.; Shahi, S.; Shrestha, L.K.; Ariga, K.; Michinobu, T. Improved Supercapacitor Performances by Adding Carbonized C_{60}-Based Nanospheres to PVA/TEMPO-Cellulose Hydrogel-Based Electrolyte. *RSC Adv.* **2023**, *13*, 21502–21509. [CrossRef]
15. Gnawali, C.L.; Shahi, S.; Manandhar, S.; Shrestha, G.K.; Adhikari, M.P.; Rajbhandari, R.; Pokharel, B.P. Porous activated carbon materials from triphala seed stones for high-performance supercapacitor applications. *BIBECHANA* **2023**, *20*, 10–20. [CrossRef]
16. Adhikari, M.P.; Shahi, S.; Ma, R.; Hill, J.P.; Ariga, K.; Shrestha, L.K. Ultrahigh Surface Area Self-Nitrogen-Doped Nanoporous Carbon Materials from *Macrotyloma uniflorum* (Horse gram) Seed for High-Performance Supercapacitor Applications. *J. Power Sources* **2025**, *631*, 236239. [CrossRef]
17. Gnawali, C.L.; Shrestha, L.K.; Hill, J.P.; Ma, R.; Ariga, K.; Adhikari, M.P.; Rajbhandari, R.; Pokharel, B.P. Nanoporous Activated Carbon Material from *Terminalia chebula* Seed for Supercapacitor Application. *C* **2023**, *9*, 109. [CrossRef]
18. Atchudan, R.; Samikannu, K.; Perumal, S.; Nesakumar, T.; Edison, J.I.; Vinodh, R.; Lee, Y.R. *Aesculus turbinata* Biomass-Originated Nanoporous Carbon for Energy Storage Applications. *Mater. Lett.* **2022**, *309*, 131445. [CrossRef]
19. Zhang, Z.; Yang, W.; Wu, Y.; Yan, G.; Li, L.; Qing, Y.; Lu, X. Porous 3D Honeycomb Structure Biomass Carbon as a Supercapacitor Electrode Material to Achieve Efficient Energy Storage. *Ind. Eng. Chem. Res.* **2021**, *60*, 11079–11085. [CrossRef]
20. Wang, L.; Fu, R.; Qi, X.; Xu, J.; Li, J.; Chen, C.; Wang, K. Deashing Strategy on Biomass Carbon for Achieving High-Performance Full-Supercapacitor Electrodes. *ACS Appl. Mater. Interface* **2024**, *16*, 52663–52673. [CrossRef]
21. Arkhipova, E.A.; Novotortsev, R.Y.; Ivanov, A.S.; Maslakov, K.I.; Scavilov, S.V. Rice Husk-Derived Activated Carbon Electrode in Redox-Active Electrolyte—New Approach for Enhancing Supercapacitor Performance. *J. Energy Storage* **2022**, *55*, 105699. [CrossRef]
22. Olivares-Marín, M.; Fernández, J.A.; Lázaro, M.J.; Fernández-González, C.; Macías-García, A.; Gómez-Serrano, V.; Stoeckli, F.; Centeno, T.A. Cherry Stones as Precursor of Activated Carbons for Supercapacitors. *Mater. Chem. Phys.* **2009**, *114*, 323–327. [CrossRef]
23. Shrestha, L.K.; Shrestha, R.G.; Joshi, S.; Rajbhandari, R.; Shrestha, N.; Adhikari, M.P.; Pradhananga, R.R.; Ariga, K. Nanoarchitectonics of Nanoporous Carbon Materials from Natural Resource for Supercapacitor Application. *J. Inorg. Organomet. Polym.* **2017**, *27*, S48–S56. [CrossRef]
24. Joshi, S.; Shrestha, L.K.; Kamachi, Y.; Yamauchi, Y.; Adhikari, M.P.; Pokharel, B.P.; Ariga, K.; Pradhananga, R.R. Sodium Hydroxide Activated Nanoporous Carbons Based on Lapsi Seed Stone. *J. Nanosci. Nanotechnol.* **2015**, *15*, 1465–1472. [CrossRef]
25. Chen, H.; Guo, Y.-C.; Wang, F.; Wang, G.; Qi, P.-R.; Guo, X.-H.; Dai, B.; Yu, F. An Activated Carbon Derived from TobaccoWaste for use as a Supercapacitor Electrode Material. *New Carbon Mater.* **2017**, *32*, 592–599. [CrossRef]
26. Torrarit, P.; Poompradub, S.; Mohammadifar, M.; Pattananuwat, P.; Jayaraman, T.; Jeong, Y.; Chanlek, N.; Choi, M.Y.; Kasemchainan, J. Highly Porous Activated Carbon from Betel Palm Shells as the Prospective Electrode for High-Performance Supercapacitors. *Mater. Sci. Energy Technol.* **2025**, *8*, 143–153. [CrossRef]
27. Ouahabi, H.E.; Elmouwahidi, A.; Cano-Casanova, L.; Lillo-Ródenas, M.A.; Roman-Martínez, M.C.; Pérez-Cadenas, A.F.; Bailón-García, E.; Shaban, M.; Al-Senani, G.M.; Ouzzine, M.; et al. From Nutshells to Energy Cells: Pioneering Supercapacitor Electrodes via Innovative Argan Nutshell Activated Carbon Synthesis. *J. Energy Storage* **2024**, *82*, 110598. [CrossRef]
28. He, X.; Ma, R.; Feng, P.; Wang, H.; Ai, L.; Xu, M.; Jia, D.; Wang, L.; Guo, N. Synthesis of Linear Amylose-Based Porous Carbon via Low-Dosage KOH Activation for High-Performance Supercapacitors. *Int. J. Biol. Macromol.* **2025**, *328*, 147685. [CrossRef] [PubMed]
29. Ruan, C.; Ai, K.; Lu, L. Biomass-Derived Carbon Materials for High-Performance Supercapacitor Electrodes. *RSC Adv.* **2014**, *4*, 30887–30895. [CrossRef]
30. Shrestha, L.K.; Shrestha, R.G.; Maji, S.; Pokharel, B.P.; Rajbhandari, R.; Shrestha, R.L.; Pradhananga, R.R.; Hill, J.P.; Ariga, K. High Surface Area Nanoporous Graphitic Carbon Materials Derived from Lapsi Seed with Enhanced Supercapacitance. *Nanomaterials* **2020**, *10*, 728. [CrossRef]
31. Chaiammart, N.; Vignesh, V.; Thu, M.M.; Eiad-ua, A.; Maiyalagan, T.; Panomsuwan, G. Chemically Activated Carbons Derived from Cashew Nut Shells as Potential Electrode Materials for Electrochemical Supercapacitors. *Carbon Resour. Convers.* **2025**, *8*, 100267. [CrossRef]
32. Manandhar, S.; Gnawali, C.L.; Rajbhandari, R.; Ma, R.; Hill, J.P.; Ariga, K.; Shrestha, L.K. Enhanced Supercapacitance Performance of Hierarchically Porous Carbon Obtained from Terminalia bellirica (Barro) Seed Stone. *ACS Appl. Energy Mater.* **2025**, *8*, 8100–8109. [CrossRef]

33. Xu, F.; Yu, J.; Tesso, T.; Dowell, F.; Wang, D. Qualitative and Quantitative Analysis of Lignocellulosic Biomass using Infrared Techniques: A Mini-Review. *Appl. Energy* **2013**, *104*, 801–809. [CrossRef]
34. Varol, E.A.; Mutlu, Ü. TGA-FTIR Analysis of Biomass Samples Based on the Thermal Decomposition Behavior of Hemicellulose, Cellulose, and Lignin. *Energies* **2023**, *16*, 3674. [CrossRef]
35. McCall, M.A.; Watson, J.S.; Tan, J.S.W.; Sephton, M.A. Biochar Stability Revealed by FTIR and Machine Learning. *ACS Sustain. Resour. Manag.* **2025**, *2*, 842–852. [CrossRef] [PubMed]
36. Tsaousis, P.C.; Sarafidou, M.; Beobide, A.S.; Mathioudakis, G.N.; Filippi, K.; Bartzialis, D.; Andrikopoulos, K.S.; Giannoulis, K.D.; Danalatos, N.G.; Koutinas, A.A.; et al. Quantification of Plant Biomass Composition via a Single FTIR Absorption Spectrum Supported by Reference Component Extraction/Isolation Protocols. *Biomass Convers. Biorefin.* **2025**, *15*, 25273–25288.
37. Wang, G.; Dai, G.; Ding, S.; Wu, J.; Wang, S. A New Insight into Pyrolysis Mechanism of Three Typical Actual Biomass: The Influence of Structural Differences on Pyrolysis Process. *J. Anal. Appl. Pyrolysis* **2021**, *156*, 105184. [CrossRef]
38. Golden, T.C.; Sircar, S. Activated Carbon Adsorbent for PSA Driers. *Carbon* **1990**, *28*, 683–690. [CrossRef]
39. Schneider, P.; Hudec, P.; Solcova, O. Pore-Volume and Surface Area in Microporous–Mesoporous Solids. *Microporous Mesoporous Mater.* **2008**, *115*, 491–496. [CrossRef]
40. Brandao, A.T.S.C.; State, S.; Costa, R.; Potorac, P.; Vazquez, J.A.; Valcarcel, J.; Silva, A.F.; Anicai, L.; Enachescu, M.; Pereira, C.M. Renewable Carbon Materials as Electrodes for High-Performance Supercapacitors: From Marine Biowaste to High Specific Surface Area Porous Biocarbons. *ACS Omega* **2023**, *8*, 18782–18798. [CrossRef]
41. Harris, P.J.F. New Perspective on the Structure of Graphitic Carbons. *Crit. Rev. Solid State Mater. Sci.* **2005**, *30*, 235–253. [CrossRef]
42. Lee, S.-M.; Lee, S.-H.; Roh, J.-S. Analysis of Activation Process of Carbon Black Based on Structural Parameters Obtained by XRD Analysis. *Crystals* **2021**, *11*, 153. [CrossRef]
43. Thangavel, R.; Kaliyappan, K.; Ramasamy, H.V.; Sun, X.; Lee, Y.S. Engineering the Pores of Biomass-Derived Carbons: Insights for Achieving Ultrahigh Stability at High Power in High-Energy Supercapacitors. *ChemSusChem* **2017**, *10*, 2805–2815. [CrossRef]
44. Miller, J.R.; Simon, P. Materials Science -Electrochemical Capacitors for Energy, Management. *Science* **2008**, *321*, 651–652. [CrossRef]
45. Yang, Z.; Ren, J.; Zhang, Z.; Chen, X.; Guan, G.; Qiu, L.; Zhang, Y.; Peng, H. Recent Advancement of Nanostructured Carbon for Energy Applications. *Chem. Rev.* **2015**, *115*, 5159–5223. [CrossRef]
46. Yang, Y.; Chen, D.; Han, W.; Cheng, Y.; Sun, B.; Hou, C.; Zhao, G.; Liu, D.; Chen, G.; Han, J.; et al. Nature-Inspired Self-Activation Method for the Controllable Synthesis of Highly Porous Carbons for High-Performance Supercapacitors. *Carbon* **2023**, *205*, 1–9. [CrossRef]
47. Huang, J.; Zhao, B.; Liu, T.; Mou, J.; Jiang, Z.; Liu, J.; Li, H.; Liu, M. Wood-Derived Materials for Advanced Electrochemical Energy Storage Devices. *Adv. Funct. Mater.* **2019**, *29*, 1902255. [CrossRef]
48. Chang, P.; Zhang, J.; Cen, Y.; Yang, F.; Li, X.; Xie, Q.; Dong, J. 3D Hierarchical Porous Carbon from Fulvic Acid Biomass for High Energy Density Supercapacitor with High Withstanding Voltage. *J. Power Sources* **2022**, *533*, 231413. [CrossRef]
49. Aziz, S.B.; Hama, P.O.; Aziz, D.M.; Sadiq, N.M.; Woo, H.J.; Kadir, M.F.Z.; Abdulwahid, R.T.; Al-Asbahi, B.A.; Ahmed, A.A.A.; Hassan, J. EDLC Supercapacitor with Enhanced Charge-Discharge Cycles Designed from Plasticized Biopolymer Blend Electrolytes: Biomaterials will be the Future of Energy Storage Devices. *J. Energy Storage* **2025**, *114*, 115841. [CrossRef]
50. Wang, H.; Ruan, F.; Feng, Q.; Liu, Y.; Wang, H. Preparation of Biomass-Derived Activated Carbon from Golden Needle Mushroom Roots for Supercapacitor Electrodes. *Mater. Lett.* **2024**, *368*, 136644. [CrossRef]
51. Shrestha, R.G.; Maji, S.; Mallick, A.K.; Jha, A.; Shrestha, R.M.; Rajbhandari, R.; Hill, J.P.; Ariga, K.; Shrestha, L.K. Hierarchically Porous Carbon Materials from *Phoenix Dactylifera* Seed for High-Performance Supercapacitor Applications. *Bull. Chem. Soc. Jpn.* **2022**, *95*, 1060–1067. [CrossRef]
52. Zhang, S.; Li, Y.; Du, Y.; Ma, X.; Lin, J.; Chen, S. Apple-Pomace-Based Porous Biochar as Electrode Materials for Supercapacitors. *Diam. Relat. Mater.* **2022**, *130*, 109507. [CrossRef]
53. Prasankumar, T.; Salpekar, D.; Bhattacharyya, S.; Manoharan, K.; Yadav, R.M.; Mata, M.A.C.; Miller, K.A.; Vajtai, R.; Jose, S.; Roy, S.; et al. Biomass Derived Hierarchical Porous Carbon for Supercapacitor Application and Dilute Stream CO_2 Capture. *Carbon* **2022**, *199*, 249–257. [CrossRef]
54. Zhang, G.; Bai, Q.; Wang, X.; Li, C.; Uyama, H.; Shen, Y. Preparation and Mechanism Investigation of Walnut Shell-Based Hierarchical Porous Carbon for Supercapacitors. *Bull. Chem. Soc. Jpn.* **2023**, *96*, 190–197. [CrossRef]
55. Liu, H.; Chen, W.; Zhang, R.; Ren, Y. Naturally O-N-S Co-Doped Carbon with Multiscale Pore Architecture Derived from Lotus Leaf Stem for High-Performance Supercapacitors. *Bull. Chem. Soc. Jpn.* **2021**, *94*, 1705–1714. [CrossRef]
56. Lobato-peralta, D.R.; Duque-Brito, E.; Orugba, H.O.; Arias, D.M.; Cuentas-Gallegos, A.K.; Okolie, J.A.; Okoye, P.U. Sponge-like Nanoporous Activated Carbon from Corn Husk as a Sustainable and Highly Stable Supercapacitor Electrode for Energy Storage. *Diam. Relat. Mater.* **2023**, *138*, 110176. [CrossRef]
57. Tu, J.; Qiao, Z.; Wang, Y.; Li, G.; Zhang, X.; Li, G.; Ruan, D. American Ginseng Biowaste-Derived Activated Carbon for High-Performance Supercapacitors. *Intl. J. Electrochem. Sci.* **2023**, *18*, 16–24. [CrossRef]

58. Wang, J.; Zhang, Q.; Deng, M. Eco-Friendly Preparation of Biomass-Derived Porous Carbon and its Electrochemical Properties. *ACS Omega* **2022**, *7*, 22689–22697. [CrossRef]
59. Wang, J.; Yang, H.; Feng, Y.; Gao, X.; Zhou, C.; Cong, S.; Ke, S. High-performance Supercapacitor Electrodes from Porous Rotten Wood Cellulose-derived Carbon via Fungi Action. *Chem. Lett.* **2023**, *52*, 389–392. [CrossRef]
60. Shrestha, R.L.; Chaudhary, R.; Shrestha, T.; Tamrakar, B.M.; Shrestha, R.G.; Maji, S.; Hill, J.P.; Ariga, K.; Shrestha, L.K. Nanoarchitectonics of Lotus Seed Derived Nanoporous Carbon Materials for Supercapacitor Applications. *Materials* **2020**, *13*, 5434. [CrossRef] [PubMed]
61. Chaudhary, R.; Maji, S.; Shrestha, R.G.; Shrestha, R.L.; Shrestha, T.; Ariga, K.; Shrestha, L.K. Jackfruit Seed-Derived Nanoporous Carbons as the Electrode Material for Supercapacitors. *C J. Carbon Res.* **2020**, *6*, 73. [CrossRef]
62. Gao, F.; Zhang, J.; Ren, M.; Ge, Y.; Chen, H.; Ma, X.; Hao, Q. Preparation and Characterization of Porous Carbons by Pyrolysis-CO_2 Gasification of Pine Sawdust. *Chem. Lett.* **2020**, *49*, 652–655. [CrossRef]
63. Gehrke, V.; Maron, G.K.; Rodrigues, L.D.S.; Alano, J.H.; Pereira, C.M.P.D.; Orlandi, M.O.; Carreño, N.L.V. Facile Preparation of a Novel Biomass-Derived H_3PO_4 and $Mn(NO_3)_2$ Activated Carbon from Citrus Bergamia Peels for High-Performance Supercapacitors. *Mater. Today Commun.* **2021**, *26*, 101779. [CrossRef]
64. Selvaraj, A.R.; Muthusamy, A.; Cho, I.; Kim, H.-J.; Senthil, K.; Prabakar, K. Ultrahigh Surface Area Biomass Derived 3D Hierarchical Porous Carbon Nanosheet Electrodes for High Energy density Supercapacitors. *Carbon* **2021**, *174*, 463. [CrossRef]
65. Song, Y.; Qu, W.; He, Y.; Yang, H.; Du, M.; Wang, A.; Yang, Q.; Chen, Y.Q. Synthesis and Processing Optimization of N-doped Hierarchical Porous Carbon Derived from Corncob for High Performance Supercapacitors. *J. Energy Storage* **2020**, *32*, 101877. [CrossRef]
66. Liu, Y.; Shi, Z.; Gao, Y.; An, W.; Cao, Z.; Liu, J. Biomass-Swelling Assisted Synthesis of Hierarchical Porous Carbon Fibers for Supercapacitor Electrodes. *ACS Appl. Mater. Interfaces* **2016**, *8*, 28283–28290. [CrossRef] [PubMed]
67. Jiang, Y.; Zhang, Z.; Zhang, Y.; Zhou, X.; Wang, L.; Yasin, A.; Zhang, L. Bioresource Derived Porous Carbon from Cottonseed Huss for Removal of Triclosan and Electrochemical Application. *RSC Adv.* **2018**, *8*, 42405–42414. [CrossRef]
68. Zhu, Y.; Chen, M.; Zhang, Y.; Zhao, W.; Wang, C. A Biomass-Derived Nitrogen-doped Porous Carbon for High-Energy Supercapacitor. *Carbon* **2018**, *140*, 404–412. [CrossRef]
69. Cao, M.; Wang, Q.; Cheng, W.; Huan, S.; Hu, Y.; Niu, Z.; Han, G.; Cheng, H.; Wang, G. A Novel Strategy Combining Electrospraying and One-Step Carbonization for the Preparation of Ultralight Honeycomb-Like Multilayered Carbon from Biomass-Derived Lignin. *Carbon* **2021**, *179*, 68–79. [CrossRef]
70. Mei, B.A.; Munteshari, O.; Lau, J.; Dunn, B.; Pilon, L. Physical Interpretations of Nyquist Plots for EDLC Electrodes and Devices. *J. Phys. Chem. C* **2018**, *122*, 194–206. [CrossRef]
71. Misnon, I.I.; Zain, N.K.M.; Jose, R. Conversion of Oil Palm Kernel Shell Biomass to Activated Carbon for Supercapacitor Electrode Application. *Waste Biomass Valor.* **2019**, *10*, 1731–1740. [CrossRef]
72. Abbas, S.C.; Lin, C.; Hua, Z.; Deng, Q.; Huang, H.; Ni, Y.; Cao, S.; Ma, X. Bamboo-Derived Carbon Material Inherently Doped with SiC and Nitrogen for Flexible Supercapacitors. *Chem. Eng. J.* **2022**, *433*, 133738. [CrossRef]
73. Jiang, Y.; He, Z.; Cui, X.; Liu, Z.; Wan, J.; Liu, Y.; Ma, F. Hierarchical Porous Carbon Derived from Coal Tar Pitch by One Step Carbonization and Activation Combined with a CaO Template for Supercapacitors. *New J. Chem.* **2022**, *46*, 6078–6090. [CrossRef]
74. Chen, K.; Weng, S.; Lu, J.; Gu, J.; Chen, G.; Hu, O.; Jiang, X.; Hou, L. Facile Synthesis of Chitosan Derived Heteroatoms-Doped Hierarchical Porous Carbon for Supercapacitors. *Microporous Mesoporous Mater.* **2021**, *320*, 111106. [CrossRef]
75. Liu, Y.; Chen, L.; Wang, Y.; Bai, Y.; Lv, Y.; Wan, L.; Hu, J.; Gan, L.; Wang, X.; Sun, J.; et al. Molten Salt Activated Biomass-Derived N/O-Dual Doped Porous Carbon for High-Performance Supercapacitors. *Diam. Relat. Mater.* **2025**, *158*, 112680. [CrossRef]
76. Nguyen, T.B.; Yoon, B.; Nguyen, T.D.; Oh, E.; Ma, Y.; Wang, M.; Suhr, J. A Facile Salt-Templating Synthesis Route of Bamboo-Derived Hierarchical Porous Carbon for Supercapacitor Applications. *Carbon* **2023**, *206*, 383–391. [CrossRef]
77. Karnan, M.; Subramani, K.; Sudhan, N.; Ilayaraja, N.; Sathish, M. Aloe vera Derived Activated High-Surface-Area Carbon for Flexible and High-Energy Supercapacitors. *ACS Appl. Mater. Interfaces* **2016**, *8*, 35191–35202. [CrossRef]
78. Charoensook, K.; Huang, C.L.; Tai, H.C.; Lanjapalli, V.V.K.; Chiang, L.M.; Hosseini, S.; Lin, Y.T.; Li, Y.Y. Preparation of Porous Nitrogen-Doped Activated Carbon Derived from Rice Straw for High-Performance Supercapacitor Application. *J. Taiwan Inst. Chem. Eng.* **2021**, *120*, 246–256. [CrossRef]
79. Wu, L.; Cai, Y.; Wang, S.; Li, Z. Doping of Nitrogen into Biomass-Derived Porous Carbon with Large Surface Area using N_2 Non-Thermal Plasma Technique for High-Performance Supercapacitor. *Int. J. Hydrogen Energy* **2021**, *46*, 2432–2444. [CrossRef]
80. Deshpande, A.; Rawat, S.; Patil, I.M.; Rane, S.; Bhaskar, T.; Ogale, S.B.; Hotha, S. Converting Renewable Saccharides to Heteroatom Doped Porous Carbons as Supercapacitor Electrodes. *Carbon* **2023**, *214*, 118368. [CrossRef]
81. Phiri, J.; Dou, J.; Vuorinen, T.; Gane, P.A.C.; Maloney, T.C. Highly Porous Willow Wood-Derived Activated Carbon for High-Performance Supercapacitor Electrodes. *ACS Omega* **2019**, *4*, 18108–18117. [CrossRef] [PubMed]
82. Zhu, M.; Yang, Y. An Electrostatic Self-Assembly Strategy to Construct Highly Stable MXene/CuO Nanocomposites for High Performance Supercapacitors. *New J. Chem.* **2025**, *49*, 5565–5569. [CrossRef]

83. Zhu, M.; Yang, Y.; Zhang, K.; Li, S. Vertically Oriented NiCoMo Sulfide Nanosheet Arrays on Ti3C2Tx MXene for High-Performance Supercapacitors. *Inorg. Chem. Front.* **2025**, *12*, 6101–6112.
84. Yang, M.; Zhang, Y.; Li, W.; Ye, P.; Nie, Y.; Zhu, M.; Li, S. Hierarchical 2D Cu-MOF@Graphene-Based Hybrids for Supercapacitor Electrodes. *Nanomaterials* **2025**, *15*, 1628. [CrossRef]
85. Li, S.; Zhang, L.; Ye, P.; Zhu, M.; Nie, Y.; Dai, Y.; Yant, F. Construction of Battery-Like Hierarchical MOF@MXene Heterostructures for Hybrid Supercapacitors. *Cryst. Growth Des.* **2024**, *24*, 7445–7454.
86. Mulik, S.V.; Koyale, P.A.; Soni, S.S.; Maske, S.M.; Dongale, T.D.; Sutar, S.S.; Parale, V.G.; Park, H.-H.; Delekar, S.D. Optimized Fabrication of Supercapacitor Using MOF-Derived $NiCo_2O_4$ with Porous Carbon as Cathode: Electrochemical Characterization and Stability Analysis using Time Series Analysis Technique. *ACS Appl. Electron. Mater.* **2024**, *6*, 4369–4380.